Magnetic Resonance Imaging 56 (2019) 90–95

Contents lists available at ScienceDirect

Magnetic Resonance Imaging

journal homepage: www.elsevier.com/locate/mri

Original contribution

Preliminary evaluation of accelerated microscopic diffusional kurtosis imaging (μDKI) in a rodent model of epilepsy

Yang Ji[a,b], Dongshuang Lu[b], Limin Wu[c], Bensheng Qiu[a], Yi-Qiao Song[b,d], Phillip Zhe Sun[b,e,f,*]

[a] Center for Biomedical Engineering, Department of Electronic Science and Technology, University of Science and Technology of China, Hefei, China
[b] Athinoula A. Martinos Center for Biomedical Imaging, Department of Radiology, Massachusetts General Hospital, Harvard Medical School, Charlestown, MA, United States of America
[c] Neuroscience Center, Department of Pediatrics, Massachusetts General Hospital, Harvard Medical School, Charlestown, MA, United States of America
[d] Schlumberger-Doll Research Center, Cambridge, MA, United States of America
[e] Yerkes Imaging Center, Yerkes National Primate Research Center, Emory University, Atlanta, GA, United States of America
[f] Department of Radiology and Imaging Sciences, Emory University School of Medicine, Atlanta, GA, United States of America

A B S T R A C T

Purpose: Our study aimed to develop accelerated microscopic diffusional kurtosis imaging (μDKI) and preliminarily evaluated it in a rodent model of chronic epilepsy.
Methods: We investigated two μDKI acceleration schemes of reduced sampling density and angular range in a phantom and wild-type rats, and further tested μDKI method in pilocarpine-induced epilepsy rats using a 4.7 Tesla MRI. Single slice average μD_{app} and μK_{app} maps were derived, and Nissl staining was obtained.
Results: The kurtosis maps from two accelerated μDKI sampling schemes (sampling density and range) are very similar to that using fully sampled data (SSIM > 0.95). For the epileptic models, μDKI showed noticeably different contrast from those obtained with conventional DKI. Specifically, the average μK_{app} was significantly less than that of the average of K_{app} (0.15 ± 0.01 vs. 0.47 ± 0.02) in the ventricle.
Conclusions: Our study demonstrated the feasibility of accelerated in vivo μDKI. Our work revealed that μDKI provides complementary information to conventional DKI method, suggesting that advanced DKI sequences are promising to elucidate tissue microstructure in neurological diseases.

1. Introduction

Diffusional kurtosis imaging (DKI) measures the degree of non-Gaussian diffusion and has been increasingly used for neuroimaging [1,2]. DKI reveals sub-voxel tissue heterogeneity and complexity in central nervous system disorders including epilepsy, Alzheimer's disease (AD) and stroke [3–7]. For example, DKI refines the heterogeneous diffusion-weighted imaging (DWI) lesion that is associated with graded metabolic derangement, which can be used for enhanced characterization of ischemic tissue injury [8–10]. It's helpful to point that routine DKI is based on single diffusion encoding (SDE), a pair of pulsed gradients that encode the diffusional displacement. Recently, double diffusion encoding (DDE) MRI has shown promise to extract important information that could not be easily inferred from the SDE experiments [10–17]. For instance, angular DDE can quantify microscopic properties affecting the spin's diffusion, including estimation of cell size [18,19], pore diameter [20], and microscopic anisotropy [16,21–23].

The routine kurtosis measurement can arise from both restricted diffusion and diffusional heterogeneity [1,24]. Recently, microscopic diffusional kurtosis imaging (μDKI) based on symmetrized DDE (s-DDE) echo planar imaging (EPI) has been demonstrated by Ji et al. [25]. In vivo μDKI displayed some unique image features that complement conventional DKI. However, the initial μDKI scan required diffusion sampling along a large number of directions, resulting in a prolonged acquisition time. Efficient μDKI acquisition and processing schemes are necessary in order to expedite its translation to the routine in vivo applications. The current work aimed to shorten the scan time of μDKI by reducing the sampling density and range of the modulation angle. Of note, cerebral atrophy is associated with epilepsy, resulting in noticeable diffusional heterogeneity [26–28]. As a result, we preliminarily tested μDKI in a rodent model of chronic epilepsy and evaluated its potential diagnostic value.

2. Material and methods

2.1. Phantom

The μDKI was tested using a three-compartment phantom. The left

* Corresponding author at: Yerkes Imaging Center, Yerkes National Primate Research Center, Emory University, Department of Radiology and Imaging Sciences, Emory University School of Medicine, 954 Gatewood Road NE, Atlanta, GA 30329, United States of America.
E-mail address: pzhesun@emory.edu (P.Z. Sun).

https://doi.org/10.1016/j.mri.2018.10.009
Received 17 August 2018; Received in revised form 15 October 2018; Accepted 18 October 2018

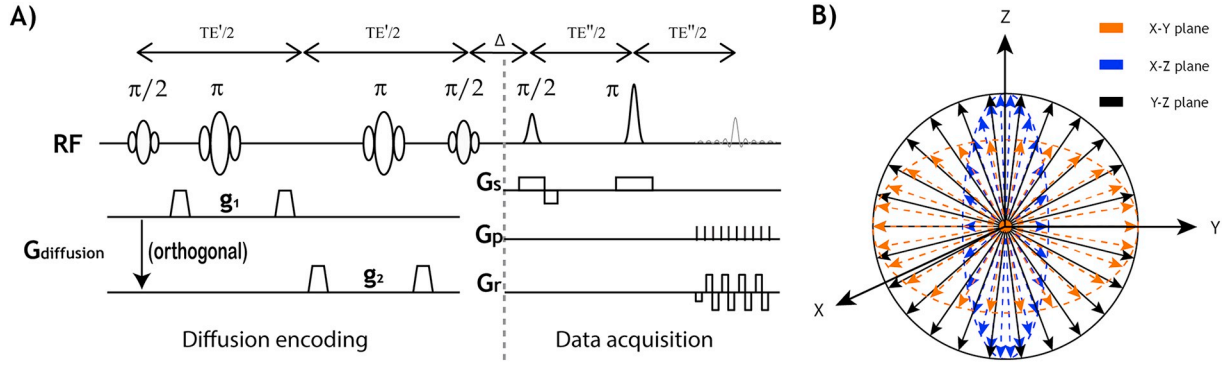

Fig. 1. The diagrams of the μDKI pulse sequence. A) Two pairs of diffusion gradients ($\mathbf{g_1}$ and $\mathbf{g_2}$) are orthogonal to one another, with their magnitudes modulated by the trigonometry of angle ϕ. B) The μDKI diffusion sampling scheme used in our study. The arrows indicate the directions of the 78 independent vectors $\vec{\mathbf{q}} = \gamma g\delta(\, g\cdot\cos(\phi)\vec{\mathbf{e}_1} + g\cdot\sin(\phi)\vec{\mathbf{e}_2})$, which are uniformly distributed in x-y, x-z, and y-z planes.

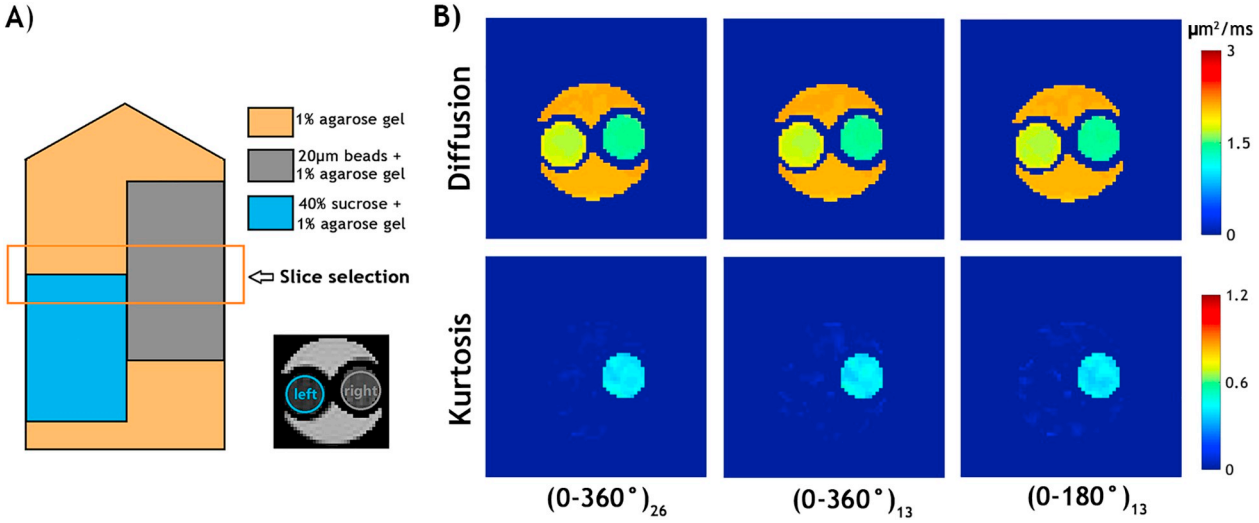

Fig. 2. Phantom validation of the expedited μDKI. A) A schematic illustration of the triple-compartment diffusion phantom. B) Diffusion and kurtosis maps obtained from three sampling schemes of μDKI, 0 to 360° with 26 steps (i.e., $(0–360°)_{26}$), 0 to 360° with 13 steps (i.e., $(0–360°)_{13}$) and 0 to 180° with 13 steps (i.e., $(0–180°)_{13}$).

centrifugal tube comprised 40% sucrose mixed with 1% agarose and 1% agarose alone, representing two superimposed Gaussian diffusion pools. The right centrifugal tube comprised 20 μm monosphere acrylic beads (MX-2000, Esprix Technologies, Sarasota, FL) mixed with 1% agarose. The third compartment (the space between two centrifugal tubes) was filled with 1% agarose gel.

2.2. Animal model of temporal lobe epilepsy

In vivo experiments have been approved by the local Institutional Animal Care and Use Committee. Adult male Sprague-Dawley (Harlan/Envigo, Indianapolis, IN) were divided into a control group ($n = 5$) and a lithium-pilocarpine-induced chronic epilepsy group ($n = 5$) [29,30]. Briefly, rats were injected intraperitoneally with 3 mmol/kg lithium chloride, followed by 1 mg/kg methylscopolamine subcutaneously after 13 h. The subcutaneous injection was repeated with 30 mg/kg pilocarpine 30 min later to trigger status epilepticus within 10–30 min. Status epilepticus was defined as continuous behavioral seizure activity scored as stage 4 or 5 according to the Racine score and lasting at least 90 min [31]. Diazepam (10 mg/kg, i.p.) was administered after 1 h of status epilepticus to terminate seizures. Repeated diazepam (5 mg/kg) was injected unless status epilepticus was terminated. Three weeks after status epilepticus, rats were video recorded (8 h/day, 5 days per week) for monitoring chronic spontaneous recurrent seizures. The chronic epilepsy model was considered successful when one or more spontaneous recurrent seizures scored as stage 3 or above according to the Racine score were observed. For the control group, lithium preconditioning was followed by saline administration instead of pilocarpine. Two months after status epilepticus, the MRI studies were performed. Rats were anesthetized with 1.5–2.0% isoflurane air during the MRI experiment. Respiratory rate and body temperature were monitored online (SA Instruments, Stony Brook, NY), and the temperature was maintained by a circulating warm water jacket positioned around the torso (Stryker Temperature Therapy Pad, Kalamazoo, MI).

2.3. MRI

MRI scans were performed using a 4.7 T small-bore Biospec MRI (Bruker, Billerica, MA) with a dual radiofrequency (RF) coil setup. For the phantom scan, μDKI was acquired with 4 b-values (0, 1000, 1500 and 2500 s/mm^2), 26 angles evenly spanning from 0 to 360° in the x-y plane (NAE = 4 and scan time = 11 min), field of view (FOV) of 50 × 50 mm^2 and 8 mm slice thickness (Matrix size = 64 × 64, repetition time (TR)/echo time (TE) = 3000/76 ms). For in vivo scans, we performed DKI using both tensor-based DKI and μDKI methods (FOV = 20 × 20 mm^2, Matrix = 64 × 64, slice thickness = 2 mm). For the standard DKI protocol, diffusion images (1000 and 2500 s/mm^2) were acquired along 30 diffusion directions in addition to a single reference image of b = 0 (δ/Δ = 4/17.5 ms, TR/TE = 3000/75.8 ms, NAE = 4, and scan time = 10 min 50 s) [32]. μDKI was acquired with 2 b-values (1000 and 2500 s/mm^2), 26 angles evenly spanning from 0 to 360° through x-y, x-z and y-z planes, respectively, in addition to a single

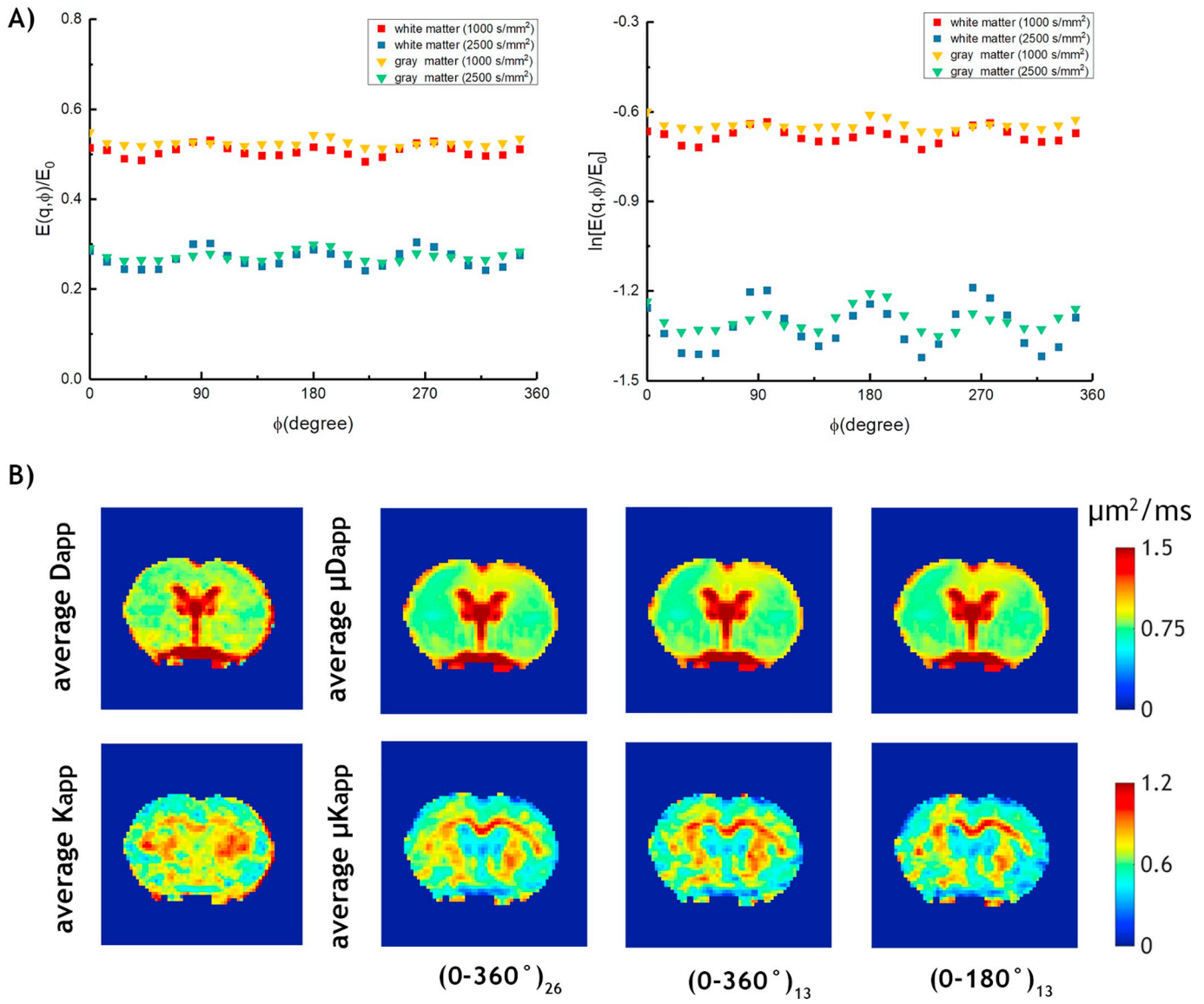

Fig. 3. Demonstration of μDKI from a representative normal rat. A) The normalized and natural logarithmic μDKI signals as a function of ϕ. B) Average Dapp and Kapp maps obtained from conventional DKI, average μDapp and μKapp maps obtained from three sampling schemes of μDKI, 0 to 360° with 26 steps (i.e., $(0–360^{\circ})_{26}$), 0 to 360° with 13 steps (i.e., $(0–360^{\circ})_{13}$) and 0 to 180° with 13 steps (i.e., $(0–180^{\circ})_{13}$).

reference image of b = 0 (NAE = 8, TR/TE = 3000/75.8 ms, and scan time = 66 min). T_2-weighted EPI images were obtained with two TE of 30 and 100 ms (TR = 3250 ms, NAE = 16). Moreover, a high-resolution rapid acquisition with relaxation enhancement (RARE) image was performed (FOV = 20 × 20 mm^2, Matrix = 128 × 128, TE = 35 ms).

2.4. Data processing

Images were processed in MATLAB (Mathworks, Natick, MA). Conventional DKI was analyzed using established routines [33,34]. For μDKI, the diffusion-induced signal can be formulated as

$$ln\left\{\frac{E(q,\phi)}{E_0}\right\} = E_{c,\tilde{0}} + E_{c,\tilde{2}}\cos(2\phi) + E_{c,\tilde{4}}\cos(4\phi) + \cdots + E_{s,\tilde{2}}\sin(2\phi) + \cdots \quad (1)$$

where $E_{c,\tilde{n}}$ and $E_{s,\tilde{n}}$ are amplitudes of nth-cycle cosine and sine terms of the natural logarithm of the μDKI signal with respect to ϕ. We investigated three sampling schemes of ϕ: 1) [0°, 360°] with intervals of 13.8°. 2) [0°, 360°] with intervals of 27.7°, and 3) [0, 180°] with intervals of 13.8°. The diffusion and kurtosis terms were calculated according to:

$$D = \frac{E_{c,\tilde{0}} - 3E_{c,\tilde{4}}}{-b} \quad (2.a)$$

$$K = \frac{4!E_{c,\tilde{4}}}{(E_{c,\tilde{0}} - 3E_{c,\tilde{4}})^2} \quad (2.b)$$

The in vivo μDKI was repeated along x-y, x-z, and y-z planes, and the diffusion and kurtosis metrics were denoted as average apparent μD (average μD_{app}) and average apparent μK (average μK_{app}), respectively. In addition, the diffusional kurtosis tensor W_{ijkl} was calculated from the tensor-based DKI approach, which was used to calculate apparent diffusion (D_{app}) and apparent kurtosis (K_{app}). To compare with μDKI, the average D_{app} and K_{app} along x-y, x-z, and y-z planes are calculated and denoted as average apparent diffusion (average D_{app}) and average apparent kurtosis (average K_{app}), respectively.

We calculated structural similarity (SSIM) index to assess the accuracy of accelerated μDKI schemes. Diffusion and kurtosis from three representative regions of interests (ROIs) of white matter (WM), gray matter (GM), and ventricle were reported as their mean ± standard

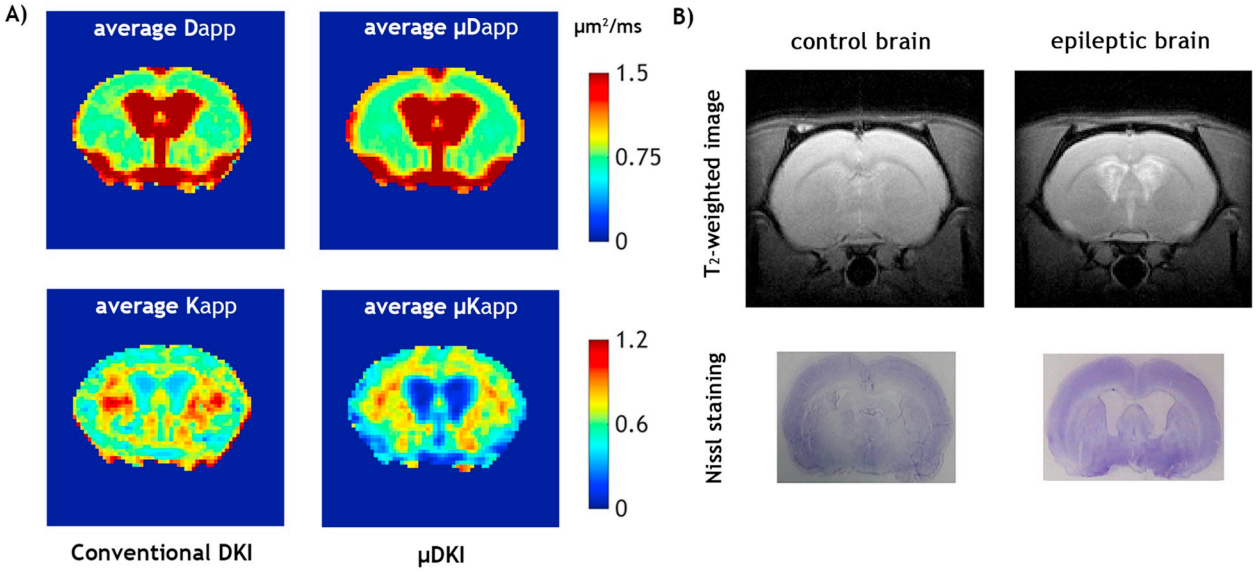

Fig. 4. Demonstration of μDKI from a representative chronic epilepsy rat. A) Comparison of diffusion and kurtosis images from the conventional DKI (average D_{app} and K_{app}) and μDKI (average μD_{app} and μK_{app}). B) T_2-weighted RARE image and the Nissl-staining from control and chronic epileptic rats.

Table 1
Comparison of in vivo conventional DKI and μDKI measurements in white matter (WM), gray matter (GM) and ventricle of wild-type and epilepsy rat brains (Mean ± SD). Paired *t*-tests were performed in control and epilepsy groups, and unpaired t-tests were performed between control and epilepsy group. A false discovery rate (FDR, $n = 6$) correction was performed. Letters in superscript (e.g., a, b) indicate the statistically significant difference between metrics.

		Control	Epilepsy
Average D_{app} ($\mu m^2/ms$)	WM	0.81 ± 0.03	0.78 ± 0.04
	GM	0.80 ± 0.04	0.82 ± 0.05
	CSF	1.89 ± 0.11[a,e]	2.81 ± 0.22[e]
Average K_{app}	WM	0.73 ± 0.06[b]	0.76 ± 0.02
	GM	0.55 ± 0.05	0.54 ± 0.03
	CSF	0.63 ± 0.09[c,f]	0.47 ± 0.02[d,f]
Average μD_{app} ($\mu m^2/ms$)	WM	0.80 ± 0.03	0.78 ± 0.03
	GM	0.82 ± 0.04	0.83 ± 0.03
	CSF	2.08 ± 0.14[a,g]	2.82 ± 0.12[g]
Average μK_{app}	WM	0.69 ± 0.04[b,h]	0.75 ± 0.02[h]
	GM	0.53 ± 0.04	0.55 ± 0.02
	CSF	0.27 ± 0.09[c,i]	0.15 ± 0.01[d,i]

[a] Significant difference between average D_{app} and average μD_{app} of CSF in the control group ($p < 0.05$).
[b] Significant difference between average K_{app} and average μK_{app} of WM in the control group ($p < 0.05$).
[c] Significant difference between average K_{app} and average μK_{app} of CSF in the control group ($p < 0.05$).
[d] Significant difference between average K_{app} and average μK_{app} of CSF in epilepsy rat group ($p < 0.05$).
[e] Significant difference of average D_{app} of CSF between control and epilepsy rat group ($p < 0.05$).
[f] Significant difference of average K_{app} of CSF between control and epilepsy rat group ($p < 0.05$).
[g] Significant difference of average μD_{app} of CSF between control and epilepsy rat group ($p < 0.05$).
[h] Significant difference of average μK_{app} of WM between control and epilepsy rat group ($p < 0.05$).
[i] Significant difference of average μK_{app} of CSF between control and epilepsy rat group ($p < 0.05$).

deviation (SD). We compared the diffusion and kurtosis indexes from conventional DKI and μDKI using two-tailed paired Student's *t*-test in control and epilepsy groups. Indices from the same ROIs were also compared using two-tailed unpaired Student's *t*-test between control and epilepsy groups. In addition, the false discovery rate (FDR, $n = 6$) correction was performed for statistical analysis. *P* values < 0.05 were considered statistically significant.

2.5. Histology

Animals were euthanized after MRI, followed by transcardial perfusion with PBS and exsanguination. Brains were dissected and frozen in 2-methylbutane on dry ice at −35 °C. Coronal cryosections were collected every 30 μm throughout the entire brain and the standard Nissl staining was performed.

3. Results

Fig. 1A shows the μDKI pulse sequence. Two pairs of diffusion gradients ($\mathbf{g}_1$ and $\mathbf{g}_2$) were applied consecutively with their relative magnitude modulated by trigonometric functions of ϕ. The echo time (TE) in μDKI sequence can be expressed as $TE = TE' + TE'' + \Delta$. In vivo μDKI was repeated with gradients along x-y, x-z and y-z plane (Fig. 1B), in which the angle ϕ spans from 0 to 360°, uniformly with intervals of 13.8° in each plane.

The accelerated μDKI schemes were first evaluated using a triple compartment phantom (Fig. 2A). Fig. 2B shows the diffusion and kurtosis maps from different sampling schemes. The original μDKI approach was denoted as $(0, 360°)_{26}$ with ϕ from 0 to 360° in 26 steps. The second scheme halved the sampling density from 26 to 13 (i.e., $(0, 360°)_{13}$) and the third scheme reduced ϕ from 0 to 360° to 0 to 180° (i.e., $(0, 180°)_{13}$). The kurtosis from the left ROI (mixed Gaussian compartment) was nearly zero from all three schemes. The kurtosis from the right ROI (monosphere beads gel compartment) showed little difference among the three approaches (0.42 ± 0.03, 0.42 ± 0.03 and 0.41 ± 0.03), with their SNR being 16.5, 13.7 and 15.2, respectively.

We then evaluated μDKI in normal rats. Fig. 3A shows signals from WM and GM as a function of ϕ for diffusion b value of 1000 and 2500 s/mm² from a representative normal rat. The signal displays a prominent 4ϕ oscillation pattern for both WM and GM. The amplitude of oscillation in WM is larger than that in GM, consistent with the fact that diffusion in WM is more restricted than that of GM [35]. Fig. 3B shows the diffusion and kurtosis maps from conventional DKI and three μDKI approaches ($(0, 360°)_{26}$, $(0, 360°)_{13}$ and $(0, 180°)_{13}$). μDKI appears to provide higher contrast between corpus callosum and cortex, consistent

with that observed in Ji et al. [25]. To compare the accelerated μDKI images, we calculated SSIM between kurtosis images derived from the two accelerated μDKI schemes with respect to that using the fully sampled μDKI data, being 0.96 ± 0.04 and 0.97 ± 0.05, respectively. This shows that accelerated μDKI schemes provide nearly identical images as the fully sampled μDKI approach.

Fig. 4A shows μDKI from a representative chronic epilepsy rat brain. The average D_{app} map from conventional DKI and the average μD_{app} map from μDKI are in good agreement with each other. In contrast, the average μK_{app} map displayed a different pattern from that of the average K_{app} map, particularly in the ventricle. Fig. 4B shows T_2-weighted RARE image and Nissl staining from control and epileptic rats. The epileptic brain had noticeable atrophy with enlarged ventricles, consistent with the chronic epilepsy model [28]. Diffusion and kurtosis values in WM, GM, and ventricle from the control and epilepsy groups were listed in Table 1. Of importance, the average μK_{app} is significantly lower than average K_{app} in CSF from the epilepsy group (0.15 ± 0.01 vs 0.47 ± 0.02, $P < 0.05$). In addition, the average μK_{app} of WM is significantly higher in the epilepsy group than that in control group (0.75 ± 0.02 vs 0.69 ± 0.04, $P < 0.05$) while the average K_{app} did not show a significant difference.

4. Discussion

μDKI is a relatively new diffusion MRI methodology that isolates compartmental kurtosis from diffusional heterogeneity. Establishment of expedited μDKI acquisition scheme is needed before it can be translated to routine preclinical and clinical applications. Our study evaluated two μDKI sampling schemes to reduce its acquisition time and validated them both in phantom and in vivo. The μDKI approach employs two pairs of gradients modulated as a function of ϕ, which needs to span a range of at least 180° with a 2-cycle modulation, per the Nyquist criterion. Indeed, our results confirmed that the acquisition time can be noticeably shortened while providing satisfactory images (SSIM > 0.95), promising for in vivo applications.

Interestingly, the μDKI shows a noticeable difference from conventional DKI in the animal model of chronic epilepsy. μK_{app} displays enlarged ventricle, consistent with cerebral atrophy in the model [27]. The average K_{app} in the ventricle is significantly higher than μK_{app}. The inflated ventricular average K_{app} is likely due to partial volume effect and/or diffusional heterogeneity. It's worth mentioning that μK_{app} was significantly different between epilepsy and control groups in WM, which is likely attributable to chronic epilepsy-induced structural changes. Indeed, it has shown that patients with temporal lobe epilepsy have diffusion abnormalities in WM [36,37]. Histopathological examinations documented disruption of myelin sheaths and altered axonal density [38]. Our results suggest that μDKI is promising to complement routine DKI for detection of microstructural changes following epilepsy.

Our study has a few limitations. First, we used a single slice μDKI pulse sequence for in vivo application. Although the μDKI pulse sequence can be extended for multi-slice readout due to the separation of s-DDE preparation and fast EPI readout, the inter-slice relaxation recovery needs to be properly accounted for. This may require correction based on relaxation measurement that is beyond the scope of our current work. Second, the s-DDE preparation was repeated in x-y, x-z, and y-z planes to estimate the average μD_{app} and μK_{app} metrics in vivo. Such an approach, strictly speaking, may not be rotationally invariant. Nevertheless, μDKI provides a reasonable estimation of tissue diffusion and kurtosis images that are clearly different from conventional DKI. Further evaluation of its diagnostic value is needed to investigate μDKI in a host of disorders including epilepsy and acute stroke.

5. Conclusion

Our study investigated accelerated μDKI acquisition and processing approaches and preliminarily demonstrated its utility in a rodent model of chronic epilepsy. The results suggest that advanced DKI complements routine diffusion MRI for improved characterization of tissue microstructure changes in neurological disorders such as epilepsy.

Acknowledgments

This study was supported in part by grants from NIH R21NS085574 and R01NS083654 to Dr. Sun and P51OD011132-58 to Yerkes National Primate Research Center.

References

[1] Jensen JH, Helpern JA, Ramani A, Lu H, Kaczynski K. Diffusional kurtosis imaging: the quantification of non-gaussian water diffusion by means of magnetic resonance imaging. Magn Reson Med 2005;53(6):1432–40.
[2] Lu H, Jensen JH, Ramani A, Helpern JA. Three-dimensional characterization of non-gaussian water diffusion in humans using diffusion kurtosis imaging. NMR Biomed 2006;19(2):236–47.
[3] Gao Y, Zhang Y, Wong CS, Wu PM, Zhang Z, Gao J, et al. Diffusion abnormalities in temporal lobes of children with temporal lobe epilepsy: a preliminary diffusional kurtosis imaging study and comparison with diffusion tensor imaging. NMR Biomed 2012;25(12):1369–77.
[4] Falangola MF, Jensen JH, Tabesh A, Hu C, Deardorff RL, Babb JS, et al. Non-Gaussian diffusion MRI assessment of brain microstructure in mild cognitive impairment and Alzheimer's disease. Magn Reson Imaging 2013;31(6):840–6.
[5] Hui ES, Fieremans E, Jensen JH, Tabesh A, Feng W, Bonilha L, et al. Stroke assessment with diffusional kurtosis imaging. Stroke 2012;43(11):2968–73.
[6] Sun PZ, Wang Y, Mandeville E, Chan ST, Lo EH, Ji X. Validation of fast diffusion kurtosis MRI for imaging acute ischemia in a rodent model of stroke. NMR Biomed 2014;27(11):1413–8.
[7] Yin J, Sun H, Wang Z, Ni H, Shen W, Sun PZ. Diffusion kurtosis imaging of acute infarction: comparison with routine diffusion and follow-up MR imaging. Radiology 2018;287(2):651–7.
[8] Cheung JS, Wang E, Lo EH, Sun PZ. Stratification of heterogeneous diffusion MRI ischemic lesion with kurtosis imaging. Stroke 2012;43(8):2252–4.
[9] Lu D, Jiang Y, Ji Y, Zhou IY, Mandeville E, Lo EH, et al. Evaluation of diffusion kurtosis imaging of stroke lesion with hemodynamic and metabolic MRI in a rodent model of acute stroke. Am J Roentgenol 2018;210(4):720–7.
[10] Wang E, Wu Y, Cheung JS, Zhou IY, Igarashi T, Zhang X, et al. pH imaging reveals worsened tissue acidification in diffusion kurtosis lesion than the kurtosis/diffusion lesion mismatch in an animal model of acute stroke. J Cereb Blood Flow Metab 2017;37(10):3325–33.
[11] Shemesh N, Jespersen SN, Alexander DC, Cohen Y, Drobnjak I, Dyrby TB, et al. Conventions and nomenclature for double diffusion encoding NMR and MRI. Magn Reson Med 2016;75(1):82–7.
[12] Lawrenz M, Finsterbusch J. Double-wave-vector diffusion-weighted imaging reveals microscopic diffusion anisotropy in the living human brain. Magn Reson Med 2013;69(4):1072–82.
[13] Shemesh N, Özarslan E, Komlosh ME, Basser PJ, Cohen Y. From single-pulsed field gradient to double-pulsed field gradient MR: gleaning new microstructural information and developing new forms of contrast in MRI. NMR Biomed 2010;23(7):757–80.
[14] Jespersen SN, Lundell H, Sønderby CK, Dyrby TB. Orientationally invariant metrics of apparent compartment eccentricity from double pulsed field gradient diffusion experiments. NMR Biomed 2013;26(12):1647–62.
[15] Shemesh N, Cohen Y. Microscopic and compartment shape anisotropies in gray and white matter revealed by angular bipolar double-PFG MR. Magn Reson Med 2011;65(5):1216–27.
[16] Özarslan E. Compartment shape anisotropy (CSA) revealed by double pulsed field gradient MR. J Magn Reson 2009;199(1):56–67.
[17] Jensen JH, Hui ES, Helpern JA. Double-pulsed diffusional kurtosis imaging. NMR Biomed 2014;27(4):363–70.
[18] Özarslan E, Komlosh M, Lizak M, Horkay F, Basser P. Double pulsed field gradient (double-PFG) MR imaging (MRI) as a means to measure the size of plant cells. Magn Reson Chem 2011;49:S79–84.
[19] Koch MA, Finsterbusch J. Compartment size estimation with double wave vector diffusion-weighted imaging. Magn Reson Med 2008;60(1):90–101.
[20] Komlosh ME, Özarslan E, Lizak MJ, Horkay F, Schram V, Shemesh N, et al. Pore diameter mapping using double pulsed-field gradient MRI and its validation using a novel glass capillary array phantom. J Magn Reson 2011;208(1):128–35.
[21] Avram AV, Özarslan E, Sarlls JE, Basser PJ. In vivo detection of microscopic anisotropy using quadruple pulsed-field gradient (qPFG) diffusion MRI on a clinical scanner. NeuroImage 2013;64:229–39.
[22] Lawrenz M, Koch MA, Finsterbusch J. A tensor model and measures of microscopic anisotropy for double-wave-vector diffusion-weighting experiments with long mixing times. J Magn Reson 2010;202(1):43–56.
[23] Shemesh N, Barazany D, Sadan O, Bar L, Zur Y, Barhum Y, et al. Mapping apparent eccentricity and residual ensemble anisotropy in the gray matter using angular double-pulsed-field-gradient MRI. Magn Reson Med 2012;68(3):794–806.
[24] Paulsen JL, Özarslan E, Komlosh ME, Basser PJ, Song YQ. Detecting compartmental non-Gaussian diffusion with symmetrized double-PFG MRI. NMR Biomed

2015;28(11):1550–6.
[25] Ji Y, Paulsen J, Zhou IY, Lu D, Machado P, Qiu B, et al. In vivo microscopic diffusional kurtosis imaging with symmetrized double diffusion encoding EPI. Magn Reson Med 2018. https://doi.org/10.1002/mrm.27419. [Epub ahead of print].
[26] Moran N, Lemieux L, Kitchen N, Fish D, Shorvon S. Extrahippocampal temporal lobe atrophy in temporal lobe epilepsy and mesial temporal sclerosis. Brain 2001;124(1):167–75.
[27] Bergmann C, Zerres K, Senderek J, Rudnik-Schöneborn S, Eggermann T, Haèusler M, et al. Oligophrenin 1 (OPHN1) gene mutation causes syndromic X-linked mental retardation with epilepsy, rostral ventricular enlargement and cerebellar hypoplasia. Brain 2003;126(7):1537–44.
[28] Weinberger DR, McClure RK. Neurotoxicity, neuroplasticity, and magnetic resonance imaging morphometry: what is happening in the schizophrenic brain? Arch Gen Psychiatry 2002;59(6):553–8.
[29] van der Hel WS, van Eijsden P, Bos IW, de Graaf RA, Behar KL, van Nieuwenhuizen O, et al. In vivo MRS and histochemistry of status epilepticus-induced hippocampal pathology in a juvenile model of temporal lobe epilepsy. NMR Biomed 2013;26(2):132–40.
[30] Wu Y, Pearce PS, Rapuano A, Hitchens TK, Ncd Lanerolle, Pan JW. Metabolic changes in early poststatus epilepticus measured by MR spectroscopy in rats. J Cereb Blood Flow Metab 2015;35(11):1862–70.
[31] Racine R, Okujava V, Chipashvili S. Modification of seizure activity by electrical stimulation: III. Mechanisms. Electroencephalogr Clin Neurophysiol 1972;32(3):295–9.
[32] Jensen JH, Helpern JA. MRI quantification of non-Gaussian water diffusion by kurtosis analysis. NMR Biomed 2010;23(7):698–710.
[33] Veraart J, Poot DH, Van Hecke W, Blockx I, Van der Linden A, Verhoye M, et al. More accurate estimation of diffusion tensor parameters using diffusion kurtosis imaging. Magn Reson Med 2011;65(1):138–45.
[34] Veraart J, Sijbers J, Sunaert S, Leemans A, Jeurissen B. Weighted linear least squares estimation of diffusion MRI parameters: strengths, limitations, and pitfalls. NeuroImage 2013;81:335–46.
[35] Fieremans E, Jensen JH, Helpern JA. White matter characterization with diffusional kurtosis imaging. NeuroImage 2011;58(1):177–88.
[36] Yogarajah M, Duncan JS. Diffusion-based magnetic resonance imaging and tractography in epilepsy. Epilepsia 2008;49(2):189–200.
[37] Gross DW. Diffusion tensor imaging in temporal lobe epilepsy. Epilepsia 2011;52:32–4.
[38] Rodríguez-Cruces R, Concha L. White matter in temporal lobe epilepsy: clinicopathological correlates of water diffusion abnormalities. Quant Imaging Med Surg 2015;5(2):264.